Determination of the fine-structure constant with an accuracy of 81 parts per trillion

Léo Morel, Zhibin Yao, Pierre Cladé, Saïda Guellati-Khélifa

Determination of the fine-structure constant with 81 parts-per-trillion accuracy

Léo Morel,[1] Zhibin Yao,[1] Pierre Cladé[1] and Saïda Guellati-Khélifa[1,2*]

[1] *Laboratoire Kastler Brossel, Sorbonne University, CNRS, ENS-PSL University, Collège de France, 4 place Jussieu, 75005 Paris, France*
[2] *Conservatoire National des Arts et Métiers, 292 rue Saint Martin, 75003 Paris, France*

The Standard Model of particle physics is remarkably successful and is consistent with (almost) all experimental results. However, it fails to explain dark matter, dark energy or the imbalance between matter and anti-matter in the universe. Any discrepancy between Standard Model predictions and experimental observations is scrutinized by physicists as it may reveal clues of new physics. An accurate evaluation of these predictions needs highly precise values of the fundamental physical constants. Among them, the fine-structure constant α has an important status in physics as it sets the strength of the electromagnetic interaction between light and charged elementary particles, such as the electron or the muon. Here we report a new determination of the fine-structure constant α^{-1}= 137.035999206 (11) with an unprecedented relative accuracy of 81 ppt (parts-per-trillion), obtained from the measurement by matter-wave interferometry of the recoil velocity of a rubidium atom that absorbs a photon. For the first time, the value of α is known with an accuracy of eleven digits which leads to a new value of the electron g-factor [1,2] - the most precise prediction of the Standard Model. Our result significantly reduces the discrepancy between the calculated electron g-factor and the direct measurement. Most notably, our new value of the fine-structure constant differs by more than 5σ from the best value available based on cesium recoil measurement [3]. It imposes new constraints on possible candidate particles from the dark sector proposed to explain the anomalous decays of excited states of ^{8}Be nuclei[4] and paves the way for testing the persistent puzzle of the magnetic moment of the muon[5] in the electron sector[6].

The fine-structure constant α is the pillar of our system of fundamental constants. As the measure of the strength of the electromagnetic interaction in the low energy limit, it has been measured using diverse physical phenomena: quantum Hall effect, Josephson effect, atomic fine structure, atomic recoil and electron magnetic moment anomaly[7]. Comparison of results across sub-fields of physics is a powerful test of the consistency between theory and the experiment. In particular, the fine-structure constant is a crucial parameter for testing quantum electrodynamics (QED) and the Standard Model (SM). This test relies on the comparison between the measured value of the electron gyromagnetic anomaly $a_e = (g_e - 2)/2$ and its theoretical value. The Standard Model prediction a_e (SM) is dominated by the QED term given by a perturbation series of (α/π). It also contains additional contributions from hadronic and weak interactions. Numerical and analytical evaluations of the coefficients of the QED series are firmly established up to the eighth order and the accuracy of the tenth-order has been improved over the last years[1,2,8]. Assuming that the prediction of the SM is correct, comparison of the theory with the most accurate measurement of the electron magnetic moment[9] leads to a value of the fine-structure constant with a relative accuracy of 2.4×10^{-10} dominated by experimental precision[9] (see Fig. 1).

From a different point of view, to test the prediction of the Standard Model, we need independent measurements of α with a similar precision to evaluate a_e(SM). The most successful independent approach is based on the measurement of the recoil velocity ($v_r = \hbar k/m$) of an atom of mass m that absorbs a photon momentum $\hbar k$[11,13]. Here $\hbar$ is the reduced Planck constant ($\hbar = h/2\pi$) and $k = 2\pi/\lambda$ is the photon wave vector (where λ is the laser wavelength). Such a measurement yields the ratio h/m and then α via the relation

$$\alpha^2 = \frac{2R_\infty}{c} \times \frac{m}{m_e} \times \frac{h}{m} \qquad (1)$$

The Rydberg constant R_∞ is determined from hydrogen spectroscopy with an accuracy of 1.9 ppt[14]. The atom-to-electron mass ratio m/m_e is obtained from the ratio of the relative atomic mass $A_r(m)$ of the atom (known at 69 ppt for rubidium[15,16]) and the relative atomic mass $A_r(m_e)$ of the electron (known at 30 ppt[17]). The speed of the light in the vacuum c has a fixed value.

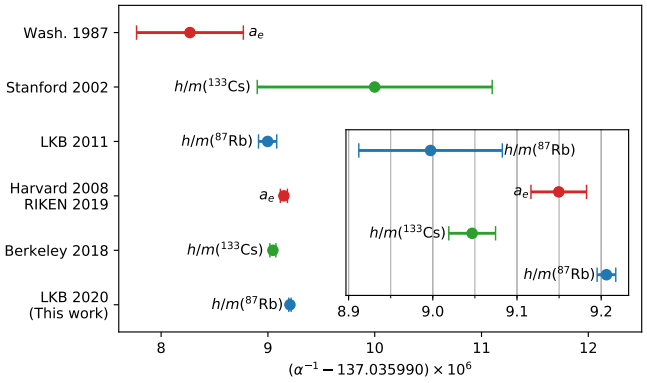

Figure 1: **Precision measurements of the fine-structure constant.** A comparison of most precise determinations of the fine-structure constant. The red points are from $g_e - 2$ measurements and QED calculations, the green and blue points are respectively obtained from the measurement of cesium and rubidium atomic recoil. Errors bars correspond to $\pm 1\sigma$ uncertainty. References: UW 1987[10], Stanford 2002[11], LKB 2011[12], Harvard 2008[9], RIKEN 2019[2], Berkeley 2018[3]

In this paper, we present a measurement of the recoil velocity on rubidium atoms. We measured $h/m_{^{87}\mathrm{Rb}} = 4.59135925890(65) \times 10^{-9}$ m^2 s^{-1}. In the international system of units adopted in 2019 where h has a fixed value, we obtain $m_{^{87}\mathrm{Rb}} = 1.44316089776(21) \times 10^{-25}$ kg. This is the most accurate atomic mass measurement. This results leads to a new determination of the fine-structure constant α:

$$\alpha^{-1} = 137.035999206(11)$$

The contribution of the uncertainty from the ratio $h/m_{^{87}\mathrm{Rb}}$ is 2.4×10^{-11} (statistical) and 6.8×10^{-11} (systematic). Our result improves the

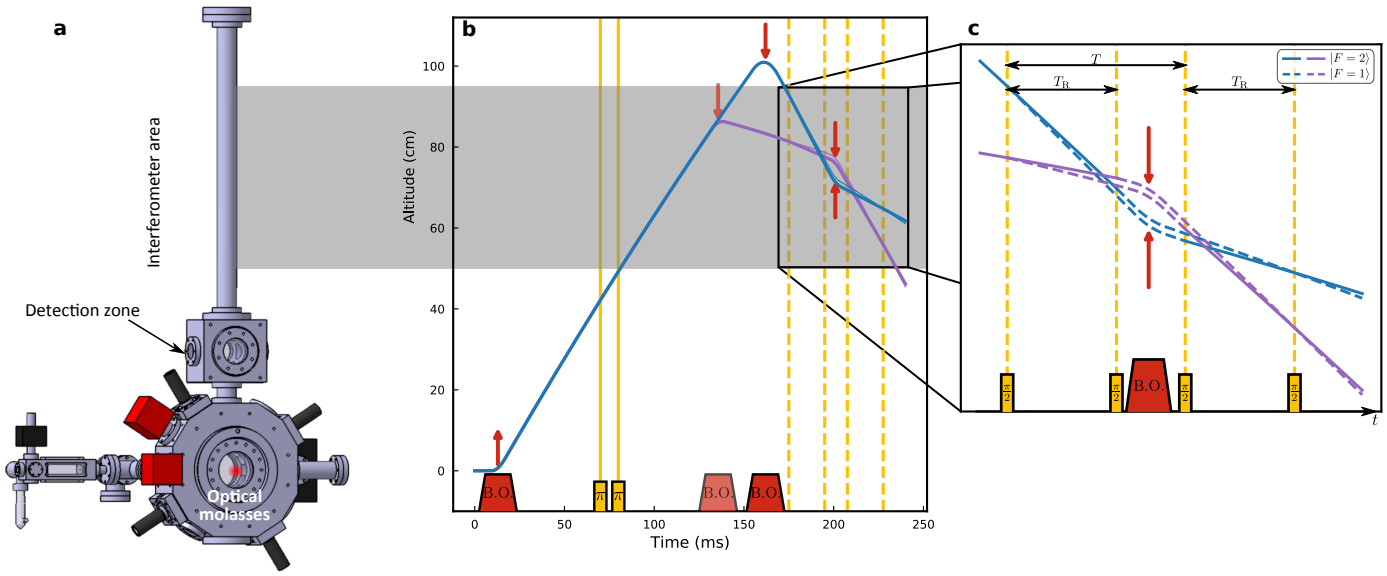

Figure 2: **Schematics of the experiment. a** Design of the vacuum chamber, the atom interferometer takes place in the upper area, a 70 cm long tube magnetically shielded. **b** Sequence of Bloch oscillations (B.O., red) and Raman pulses (yellow) used to control the trajectory of the atoms before starting the atom interferometer. **c** Atom interferometer light pulse sequence. The atomic trajectories for upwards (blue) and downwards (purple) accelerations are previously calculated to mitigate gravity gradient effect. In order to be visible, the separation between the two paths of each interferometer is exaggerated.

accuracy on α by a factor of 2.5 over the previous cesium recoil measurement[3] but most notably it reveals a 5.4 σ tension with this latest measurement.

We have built a new experimental setup and implemented robust methods to control systematic effects. Accelerating atoms up to $6\,\mathrm{m\,s^{-1}}$ in 6 ms and using usual two-photon Raman transitions as beamsplitters for the matter-waves, we obtained a relative sensitivity on the recoil velocity of 0.6 ppb in one hour of integration (0.3 ppb on α). This sensitivity is more than three times better than that obtained on the best atom interferometer based on multi-photon beamsplitters [3] although the latter technique is expected to provide a significant gain in sensitivity with respect to Raman transitions[18,19].

The unprecedented sensitivity of our atom interferometer enables us to experimentally evaluate and mitigate several systematic biases. We recorded data with different experimental parameters, reinforcing the overall confidence of our error budget. We have also implemented a Monte Carlo simulation that includes both the Ramsey-Bordé atom interferometer and the Bloch oscillations process. This code models precisely the underlying physics of our interferometer and provides accurate evaluation of systematic effects consistent with experimental results.

Experiment

Our experimental method is illustrated in Fig. 2. The basic tools of our experiment are Bloch oscillations in an accelerated optical lattice that enable to coherently transfer a precise number of photon momenta to the atoms (typically 1000 $\hbar k$), and a matter-wave interferometer that measures the phase shift due to the change in velocity of the atoms. As in the optical domain, atom interferometry needs tools to split and recombine atomic wave packets. This is accomplished by a sequence of light pulses. The probability of detecting atoms in a given internal state at the output of the interferometer is a sinusoidal function of the accumulated phase difference along the two paths. Thus, the measurement of atomic populations enables the evaluation of the phase shift. Using the combination of the Ramsey-Bordé interferometer configuration and Bloch oscillations, the phase shift is proportional to the ratio h/m[20].

We produce a cold rubidium sample using an optical molasses in the main chamber. Then atoms are transported to the interferometry area embodied by a 70 cm long tube surrounded by a two-layer magnetic shield. The magnetic field is controlled to within 50 nT. For that, we use an atomic elevator based on two Bloch oscillations pulses (acceleration/deceleration)[20]. They are performed using two vertical counter-propagating laser beams whose frequency difference is swept to create an accelerated standing wave. Atomic trajectories are precisely adjusted by controlling this frequency difference. In between the two Bloch oscillations pulses of the elevator, we apply two Raman pulses to prepare atoms in a well-defined atomic internal state (see Fig. 2b). Raman transitions occur between the two hyperfine levels of the ground state of the rubidium atom and are also implemented using two vertical counter-propagating laser beams (with wave vectors $\vec{k}_1 = -\vec{k}_2$ and $k_1 \simeq k_2 = k_\mathrm{R}$). Their frequency difference ω_R is controlled to compensate precisely the Doppler shift induced by the accelerations of the atoms.

The atom interferometer is illustrated in Fig. 2c. It is implemented with two pairs of $\pi/2$ Raman pulses. Each pulse acts as a beamsplitter by transferring to an atom a momentum of $2\hbar k_\mathrm{R}$ with probability of 50%. The first pair creates a coherent superposition of two spatially separated wave packets in the same internal state with same momentum. The second pair recombines the two wave packets. Between the second and third $\pi/2$ pulses, a Bloch oscillations pulse transfers a momentum of $2N_\mathrm{B}\hbar k_\mathrm{B}$ to both wave packets. The overall phase Φ of the interferometer is given by

$$\Phi = T_\mathrm{R}\left[\epsilon_\mathrm{R} 2k_\mathrm{R}\left(\epsilon_\mathrm{B}\frac{2N_\mathrm{B}\hbar k_\mathrm{B}}{m} - gT\right) - \delta\omega_\mathrm{R}\right] + \phi_\mathrm{LS} \qquad (2)$$

where T_R is the time between the $\pi/2$ pulses of each pair, T is the time between the first and the third $\pi/2$ pulses, g is gravity, ϕ_LS represents the phase due to parasitic atomic level shifts and $\delta\omega_\mathrm{R}$ is the difference of the Raman frequencies between the first and the third $\pi/2$ pulses. ϵ_R and ϵ_B determine respectively the orientation of Raman and Bloch lasers wave vectors.

Fluorescence signal collected in the detection zone tells us the number of atoms in each atomic level at the output of the interferometer. Atomic

fringes are obtained by measuring the fraction of atom in given internal state varying $\delta\omega_{\mathrm{R}}$. Using a mean square adjustment we calculate $\delta\omega_{\mathrm{R},0}$, the frequency for which $\Phi = 0$. Gravity is cancelled between upward ($\epsilon_{\mathrm{B}} = 1$) and downward ($\epsilon_{\mathrm{B}} = -1$) acceleration (see Fig 2). Constant levels shifts ϕ_{LS} are mitigated by inverting Raman beams direction ($\epsilon_{\mathrm{R}} = \pm 1$). The shot-to-shot parameters of the interferometer ($\delta\omega_{\mathrm{R}}, \epsilon_{\mathrm{R}}, \epsilon_{\mathrm{B}}$) are executed randomly to avoid drifts. We record four spectra (Fig. 3a) that yield

$$\frac{\hbar}{m} = \frac{1}{4}\frac{\sum_{\epsilon_{\mathrm{R}},\epsilon_{\mathrm{B}}} |\delta\omega_{\mathrm{R},0}(\epsilon_{\mathrm{R}},\epsilon_{\mathrm{B}})|}{4N_{\mathrm{B}}k_{\mathrm{B}}k_{\mathrm{R}}} \tag{3}$$

Data Analysis

For the conditions of Fig 3a, the typical uncertainty on $\delta\omega_{\mathrm{R},0}$ is 55 mHz. This leads to statistical uncertainty on h/m below 2 ppb in 5 min. The behavior of Allan deviation calculated with a set of h/m measurements over 56 hours (Fig. 3b) shows that data are independent (no correlations or long-term drift). It also tell us that the sensitivity of our setup on α, is 8×10^{-11} in 14 hours.

Table 1 presents our error budget. Several systematic effects already identified in our previous measurement[12] have been reduced by at least one order of magnitude. By controlling the experimental parameters of the atomic elevator, we are able to adjust precisely the altitude of atomic trajectories within 100 µm in such way that the gravity gradient cancels out between configurations $\epsilon_{\mathrm{B}} = 1$ and $\epsilon_{\mathrm{B}} = -1$ (see Fig 2c). The effect of Earth's rotation is suppressed by rotating continuously one of the Raman beam during the interferometric pulse sequence[21]. The long-term drift of the beams alignment is corrected with an accuracy better than 4 µrad every 45 min by controlling the retro-reflection of laser beams via a single-mode optical fiber. Our lasers are locked on a stabilized Fabry-Perot cavity and their frequencies are regularly measured using a frequency comb with an accuracy of less than 4 kHz. The low density of our atomic sample makes effects of index of refraction and atom-atom interaction[22] less than 1 part-per-trillion. Effects related to the geometrical parameters of the laser beams (Gouy phase and wave front curvature) are mitigated by utilizing a 4.9 mm beam passing through an apodizing filter and by adjusting the curvature with a shearing interferometer.

Among the new systematic effects, the most subtle is related to correlations between the efficiency of Bloch oscillations and short-scale spatial fluctuations in laser intensity. This effect raises the tricky question of the photon momentum in a distorted optical field. Relying on the work we have done in reference[23], we reduce its contribution to the error budget to less than 0.02 ppb. Because of the expansion of the atomic cloud, there is a residual phase shift which is due the variation of the intensity perceived by the atoms. This phase shift depends on the velocity distribution[24,25]. We have implemented a compensation of the mean intensity variation and use the Monte Carlo simulation to evaluate the residual bias due to this Raman phase shift.

During the interferometer sequence we apply a frequency ramp to compensate the Doppler shift induced by gravity. Non-linearity in the delay of the optical phase lock loop induces a residual phase shift that has been measured and corrected for each spectrum. These new systematic effects were not considered in our previous measurement[12] (see Fig. 1). This could explain the 2.4 σ discrepancy between our new measurement and $\alpha_{\mathrm{LKB2011}}$. Unfortunately we do not have available data to evaluate retrospectively the contributions of the phase shift in the Raman phase lock loop and of short scale fluctuations of laser intensity to the 2011 measurement. Thus, we cannot firmly state that these two effects are the cause of the 2.4 σ discrepancy between our two measurements.

Overall systematic errors contribute an uncertainty of 0.8×10^{-11}. Fig. 3c shows our data used for the determination of α. Each point represents about 10 hours of data. We took advantage of the sensitivity and reproducibility of our setup to study systematic effects by varying the experimental parameters (pulse-separation time, number of Bloch oscillations, duration of Bloch pulse, laser intensity, atomic trajectories…). In parallel, theoretical modeling and numerical simulations were performed to interpret the experimental observations. The measurement campaign lasted one year and ended when consistent values for the different configurations were obtained.

Source	Correction $[10^{-11}]$	Relative uncertainty $[10^{-11}]$
Gravity gradient	-0.6	0.1
Alignment of the beams	0.5	0.5
Coriolis acceleration		1.2
Frequencies of the lasers		0.3
Wave front curvature	0.6	0.3
Wave front distortion	3.9	1.9
Gouy phase	108.2	5.4
Residual Raman phase shift	2.3	2.3
Index of refraction	0	< 0.1
Internal interaction	0	< 0.1
Light shift (two-photon transition)	-11.0	2.3
Second order Zeeman effect		0.1
Phase shifts in Raman phase lock loop	-39.8	0.6
Global systematic effects	64.2	6.8
Statistical uncertainty		2.4
Relative mass of ^{87}Rb [16] : 86.909 180 531 0(60)		3.5
Relative mass of the electron [14] : 5.485 799 090 65(16) $\cdot 10^{-4}$		1.5
Rydberg constant [14] : 10 973 731.568 160(21)m^{-1}		0.1
Total: $\alpha^{-1} = 137.035\,999\,206(11)$		8.1

Table 1: **Error budget on α.** For each systematic effect, more discussion can be found in the listed section of the Methods.

Using our measurement of the fine-structure constant, the Standard Model prediction of the anomalous magnetic moment of the electron becomes

$$a_{\mathrm{e}}(\alpha_{\mathrm{LKB2020}}) = \frac{g_{\mathrm{e}} - 2}{2} = 1159652180.252\ (95) \times 10^{-12}$$

The relative uncertainty on g_{e} is for the first time below 0.1 part-per-trillion, this is the most accurate prediction of the Standard Model. The comparison with direct experimental measurement [9] is $\delta a_{\mathrm{e}} = a_{\mathrm{e}}(\mathrm{Exp}) - a_{\mathrm{e}}(\alpha_{\mathrm{LKB2020}}) = (4.8 \pm 3.0) \times 10^{-13}$ (+1.6 σ), while using cesium recoil measurement $\delta a_{\mathrm{e}}(\alpha_{\mathrm{Berkeley}}) = (-8.8 \pm 3.6) \times 10^{-13}$ (-2.4 σ). The uncertainty on δa_{e} is now dominated by $a_{\mathrm{e}}(\mathrm{Exp})$.

Discussion

Our measurement enables new limits to be placed on theories beyond the SM that lead to a contribution to a_{e}. Using a Bayes method[26], our result implies that for a theory where δa_{e} is positive, we can reject with a 95% confidence level $\delta a_{\mathrm{e}} > 9.8 \times 10^{-13}$ and for a theory where δa_{e} is negative, we can reject with a 95% confidence level $\delta a_e < -3.4 \times 10^{-13}$.

For example, our result places new limits on a possible substructure within the electron. If the electron is composed of constituent particles of mass m^* bound together by some unknown attraction, its natural size should be $R = \hbar/(m^* c)$ and it would manifest a modification of its magnetic moment $\delta a_e \simeq m_{\mathrm{e}}/m^*$ using the simplest analysis. According to the chirally invariant model [27] our result excludes with a confidence level of 95% regions where $m^* < 520$ GeV/c^2 or size $R > 4 \times 10^{-19}$ m. These are stringent limits set by low energy experiments, although they are not yet at the LEP (largest e^+e^- collider) limits [28].

Moreover, our result sets the stage for testing whether the persistent discrepancy of 3.6 σ between the experimental value[5] and the Standard Model prediction of the magnetic moment of the muon[29,30] exits in the electron sector. If the δa_μ discrepancy is the signature of new physics, similar effects could be observable in electron sector. Using a naive scaling, the effects on the electron will be of the order of $(m_{\mathrm{e}}/m_\mu)^2 \delta a_\mu$[6]. Fig. 4a summarizes contributions of overall experiments involved in the determination of δa_{e}. We also include the largest theoretical contributions from the fifth order of the QED series and the hadronic term. The dominant contribution comes from the Penning trap measurement. For the first time, the contribution of the recoil measurement is at the level of $(m_{\mathrm{e}}/m_\mu)^2 \delta a_\mu \simeq 6.5 \times 10^{-14}$, the value of δa_{e} deduced from the naive scaling (horizontal green bar). In the next years, improvement of one order of magnitude is expected for the measurement of a_e[31], it will then be possible to probe physics beyond the SM with comparable information from both the electron and muon.

Finally, the anomaly reported in the angular distribution of e^+e^- produced in ^{8}Be nuclear transitions[4] could be explained by the emission of a hypothetical protophobic gauge boson X with a mass of 16.7 MeV followed by a decay through X $\rightarrow e^+e^-$ [32]. The X-boson is parameterized by a mixing strength ϵ with electrons and a nonzero mass m_X. The Fig 4b represents exclusions space for those parameters. At 16.7 MeV,

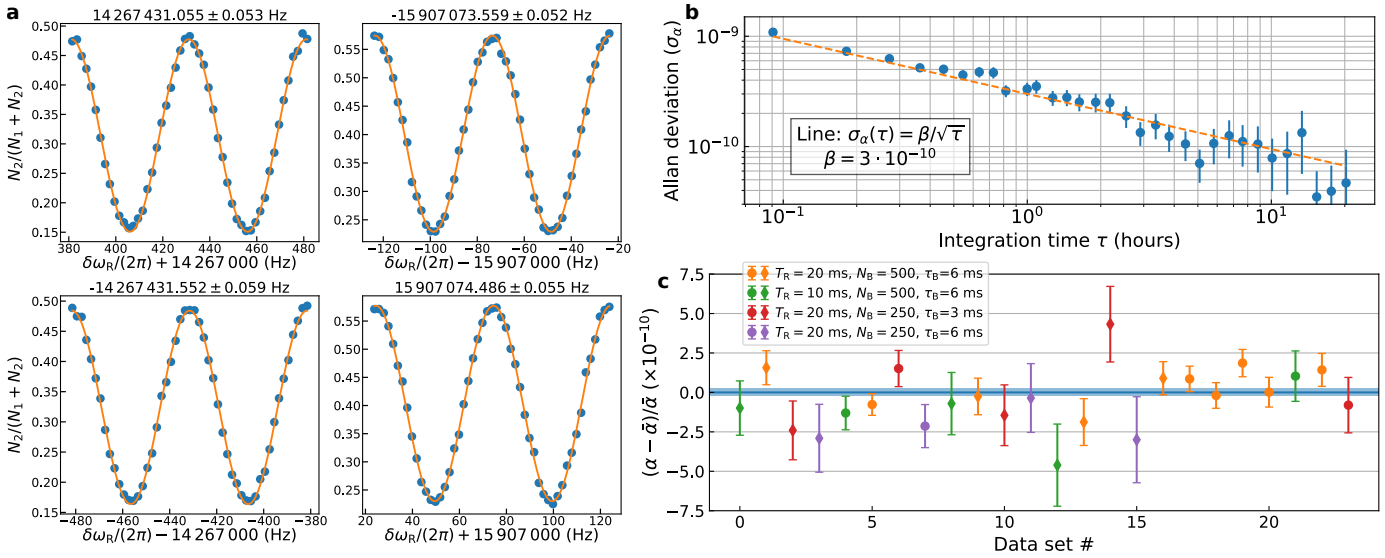

Figure 3: **Data analysis. a** Typical set of four spectra recorded by inverting directions of Raman and Bloch beams for $T_R = 20$ ms, $N_B = 500$. Each spectrum displays the variation of the relative atomic population with respect to the parameter $\delta\omega_R$. **b** Allan deviation σ_α of measurement of the fine-structure constant α at maximum sensitivity ($T_R = 20$ ms, $N_B = 500$) as a function of the integration time τ. Line : $\sigma_\alpha(\tau) = 3 \cdot 10^{-10}/\sqrt{\tau}$ with τ expressed in hours. **c** Data set used for the determination of the value of the fine-structure constant α. Data are obtained by changing experimental parameters: the pulse separation time T_R, the number of Bloch oscillations N_B and their total duration τ_B. The circles and diamonds correspond to two different laser intensities during the $\pi/2$ pulses of the interferometer. Error bar denote the $\pm 1\sigma$ and are estimated by the standard deviation of the mean. The blue band represents the overall $\pm 1\sigma$ standard deviation. The reduced χ^2 for combined data is 1.4.

the upper limit of ϵ is set by the $g_e - 2$ of the electron and its lower limit by electron beam dump experiments (E141 and NA64 collaborations). Recently, new results from NA64 collaboration[33] excluded ϵ values lower than 6.8×10^{-4}. Because a vector coupling implies $\delta a_e > 0$, the result from cesium recoil imposes strong constraints on ϵ. Combined with NA64, it rejects at 90 % C.L. purely vector coupling of X(16.7). On the contrary, our measurement of α leads to $\delta a_e > 0$ and favored a value a purely vector coupling with $\epsilon = (8 \pm 3) \times 10^{-4}$ that could explain the ^{8}Be anomaly.

Acknowledgement This work has been supported by the U.S. National Institute of Standards and Technlology (NIST) Precision Measurement Grant Program under Award Number 60NANB16D271 and by the LABEX Cluster of Excellence FIRST-TF (ANR-10-LABX-48-01), within the Program *Investissements d'Avenir* operated by the French National Research Agency (ANR). We are particularly grateful to R. Jannin and C. Courvoisier who participate actively to the construction of the experimental setup initially funded by the ANR, INAQED Project No. ANR-12-JS04-0009.

Contributions The experiment was performed by L. M, Y. Z, P. C and S. G-K. The data were analyzed by L. M, P. C and S. G-K. The manuscript was written by S. G-K and the Methods by L. M. and P. C. All authors discussed and approved the data as well as the manuscript and the Methods.

Competing interests The authors declare no competing interests.

Data availability statement The datasets generated during and/or analysed during the current study are available from the corresponding author on reasonable request.

Code availability statement The experimental data were analysed using a self-written analysis script, which is available from the corresponding author on reasonable request

Main references

1. Aoyama, T., Hayakawa, M., Kinoshita, T. & Nio, M. Tenth-Order QED Contribution to the Electron g - 2 and an Improved Value of the Fine Structure Constant. *Phys. Rev. Lett.* **109**, 111807 (2012).

2. Aoyama, T., Kinoshita, T. & Nio, M. Theory of the Anomalous Magnetic Moment of the Electron. *Atoms* **7**, 28 (2019).

3. Parker, R. H., Yu, C., Zhong, W., Estey, B. & Müller, H. Measurement of the fine-structure constant as a test of the Standard Model. *Science* **360**, 191–195 (2018).

4. Krasznahorkay, A. J. *et al.* Observation of anomalous internal pair creation in ^{8}Be: A possible indication of a light, neutral boson. *Phys. Rev. Lett.* **116**, 042501 (2016).

5. Bennett, G. W. *et al.* Final report of the E821 muon anomalous magnetic moment measurement at BNL. *Phys. Rev. D* **73**, 072003 (2006).

6. Terranova, F. & Tino, G. M. Testing the a μ anomaly in the electron sector through a precise measurement of h / M. *Phys. Rev. A* **89**, 052118 (2014).

7. Mohr, P. J., Newell, D. B. & Taylor, B. N. CODATA recommended values of the fundamental physical constants: 2014. *Rev. Mod. Phys.* **88**, 035009 (2016).

8. Laporta, S. High-precision calculation of the 4-loop contribution to the electron g -2 in QED. *Physics Letters B* **772**, 232–238 (2017).

9. Hanneke, D., Fogwell, S. & Gabrielse, G. New measurement of the electron magnetic moment and the fine structure constant. *Phys. Rev. Lett.* **100**, 120801 (2008).

10. Dyck, R. V., Schwinberg, P. & Dehmelt, H. New high-precision comparison of electron and positron g factors. *Physical Review Letters* **59**, 26 (1987).

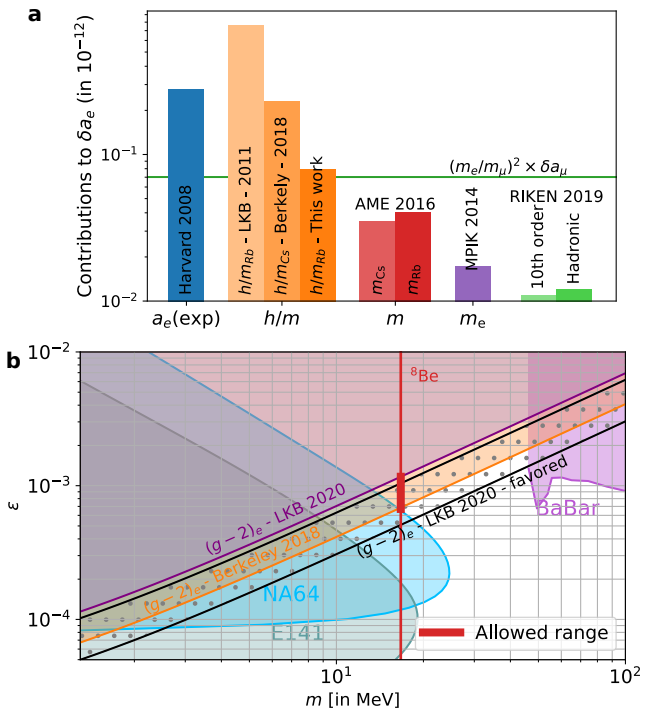

Figure 4: **Impact on the test of the Standard Model prediction of a_e and limits on hypothetical X boson. a** Summary of contributions to the relative uncertainty on δa_e. The horizontal green line corresponds to the δa_e obtained taking into account the muon discrepancy and using the naive scaling model. References: Harvard 2008[9], LKB 2011[12], Berkely 2018[3], AME 2016[16], MPIK 2014[17], RIKEN[2]. **b** Exclusion area in (ϵ, m_X) space, for the X boson.

11. Wicht, A., Hensley, J. M., Sarajlic, E. & Chu, S. A Preliminary Measurement of the Fine Structure Constant Based on Atom Interferometry. *Physica Scripta* **T102**, 82 (2002).

12. Bouchendira, R., Cladé, P., Guellati-Khélifa, S., Nez, F. & Biraben, F. New determination of the fine structure constant and test of the quantum electrodynamics. *Phys. Rev. Lett.* **106**, 080801 (2011).

13. Battesti, R. *et al.* Bloch Oscillations of Ultracold Atoms: A Tool for a Metrological Determination of h / m Rb. *Phys. Rev. Lett.* **92**, 253001 (2004).

14. CODATA recommended values of the fundamental physical constants: 2018. `https://pml.nist.gov/cuu/Constants/`.

15. Mount, B. J., Redshaw, M. & Myers, E. G. Atomic masses of Li 6 , Na 23 , K 39 , 41, Rb 85 , 87 and Cs 133. *Phys. Rev. A* **82**, 042513 (2010).

16. Huang, W. *et al.* The AME2016 atomic mass evaluation (I). Evaluation of input data; and adjustment procedures. *Chinese Phys. C* **41**, 030002 (2017).

17. Sturm, S. *et al.* High-precision measurement of the atomic mass of the electron. *Nature* **506**, 467–470 (2014).

18. Cladé, P., Guellati-Khélifa, S., Nez, F. & Biraben, F. Large Momentum Beam Splitter Using Bloch Oscillations. *Phys. Rev. Lett.* **102**, 240402 (2009).

19. Müller, H., Chiow, S.-w., Long, Q., Herrmann, S. & Chu, S. Atom Interferometry with up to 24-Photon-Momentum-Transfer Beam Splitters. *Phys. Rev. Lett.* **100**, 180405 (2008).

20. Cadoret, M. *et al.* Combination of bloch oscillations with a ramsey-bordé interferometer: New determination of the fine structure constant. *Physical Review Letters* **101**, 230801 (2008).

21. Lan, S.-Y., Kuan, P.-C., Estey, B., Haslinger, P. & Müller, H. Influence of the Coriolis Force in Atom Interferometry. *Phys. Rev. Lett.* **108**, 090402 (2012).

22. Jannin, R., Cladé, P. & Guellati-Khélifa, S. Phase shift due to atom-atom interactions in a light-pulse atom interferometer. *Phys. Rev. A* **92**, 013616 (2015).

23. Bade, S., Djadaojee, L., Andia, M., Cladé, P. & Guellati-Khelifa, S. Observation of Extra Photon Recoil in a Distorted Optical Field. *Phys. Rev. Lett.* **121**, 073603 (2018).

24. Gillot, P., Cheng, B., Merlet, S. & Pereira Dos Santos, F. Limits to the symmetry of a Mach-Zehnder-Type atom interferometer. *Physical Review A* **93** (2016).

25. Morel, L., Yao, Z., Cladé, P. & Guellati-Khélifa, S. Velocity-dependent phase shift in a light-pulse atom interferometer (2020). `arxiv: 2006.14354`.

26. Yu, C. *et al.* Atom-interferometry measurement of the fine structure constant. *Annalen der Physik* **531**, 1800346 (2019).

27. Brodsky, S. J. & Drell, S. D. Anomalous magnetic moment and limits on fermion substructure. *Phys. Rev. D* **22**, 2236–2243 (1980).

28. Bourilkov, D. Hint for axial-vector contact interactions in the data on $e^+e^- \to e^+e^-(\gamma)$ at center-of-mass energies 192–208 GeV. *Phys. Rev. D* **64**, 071701 (2001).

29. Aoyama, T., Kinoshita, T. & Nio, M. Revised and improved value of the QED tenth-order electron anomalous magnetic moment. *Phys. Rev. D* **97**, 036001 (2018).

30. Davoudiasl, H., Lee, H.-S. & Marciano, W. J. Muon g - 2 , rare kaon decays, and parity violation from dark bosons. *Phys. Rev. D* **89**, 095006 (2014).

31. Gabrielse, G., Fayer, S. E., Myers, T. G. & Fan, X. Towards an improved test of the standard Model's most precise prediction. *Atoms* **7** (2019).

32. Feng, J. L. *et al.* Protophobic fifth-force interpretation of the observed anomaly in ^{8}Be nuclear transitions. *Phys. Rev. Lett.* **117**, 071803 (2016).

33. Banerjee, D. *et al.* Improved limits on a hypothetical X(16.7) boson and a dark photon decaying into e^+e^- pairs. *Phys. Rev. D* **101**, 071101 (2020).

Methods

Experimental setup The design of the science chamber is shown on Fig. 2a. A 3D-magneto optical trap (3D-MOT) is loaded by a slow atomic beam generated in a 2D-MOT. An optical molasses is used to further cool down atoms to a temperature of 4 µK. The temperature of the atomic cloud was measured using Doppler sensitive Raman transitions.

After being released from the optical molasses ($t = 0$), atoms are transported to a separate chamber, where the vacuum is controlled at the level of few 10^{-11} mbar. It consists of a long tube placed 50 cm above the center of the MOT. One main difference with the previous setup is that the atom interferometer is realized in this separate and long tube where the magnetic field is precisely controlled thanks to a uniformly wound solenoid shielded by two layers of μ-metal.

Lasers for the Raman transitions are produced using second harmonic generation (SHG) from 1.56 µm lasers. These two lasers are phase-locked and the scheme used to control the frequency difference between the two laser during the interferometer sequence is depicted on **Extended Data Figure 3a**. The power used to drive Raman transitions is at maximum 70 mW per beam. Lasers are detuned with respect to the one photon transition (Rb D2-line) by about 60 GHz.

Laser beams for the Bloch oscillations (BOs) are produced from a 1.56 µm fiber laser that is split in two. Each beam seeds an optical system made by μQuans company where the beam passes through an acousto-optic modulator (AOM) to control their frequency, is then amplified and passes through a PPLN cristal for SHG (about 800 mW at 780 nm). The two Bloch beams are filtered through a Rb vapour cell to reduce the resonant component of the amplified spontaneous emission (ASE) of the amplifiers[34]. The total power is 400 mW for a peak intensity of 530 mW cm^{-2}. The laser is blue-detuned by 40 GHz from Rb D2-line.

The two Raman beams have a linear and orthogonal polarizations. The two Raman and one of the Bloch beams are transported with the same single mode polarization maintaining (PM) fiber at the top of the cell and point downward (**Extended Data Figure1a**). A Polarizing Beam Splitter (PBS) is placed at the bottom of the vacuum cell. It transmits one of the Raman beams which is then retro-reflected on a horizontal mirror placed on a vibration isolation table to achieve the counter-propagating configuration. The second Raman beam and the Bloch beam are rejected by the PBS. The inversion of the Raman effective wave vector is performed by rotating the polarization of the Raman beams by 90° before the fiber. The second Bloch beam is transported by an independent single mode PM fiber at the bottom of the cell and is upward. The waist of the beams at the output of the collimators is 4.9 mm. An apodizing filter is placed after each collimator[3].

Experimental sequence To transport atoms in the interferometry area, we use an atomic elevator based on two Bloch oscillations pulses (acceleration/deceleration)[20]. Adjusting the parameters of the elevator (number of Bloch oscillations and delays), we can precisely choose the initial position z_0 and velocity v_0 of the cloud at the start of the interferometer $t_{\mathrm{interf.}}$. In between the two Bloch oscillations pulses of the elevator, we apply two Raman π-pulses with a blow-away pulse in between. With this sequence atoms are prepared in the magnetically insensitive state and by controlling the parameters of the first Raman π-pulse (intensity and duration) one can set the width of the vertical velocity distribution of the atomic cloud. With a pulse duration of 189 µs, we obtain a velocity distribution whose full width at half maximum is 1.7 mm s^{-1}. After the preparation sequence, 500 000 atoms form the cloud.

The interferometer consists of four $\pi/2$ Raman pulses of same duration arranged in two identical Ramsey sequences (delay T_R) separated by a duration T. The BOs pulse is applied between the second and third Raman pulse (see Fig. 2c or **Extended Data Figure 1c** where the notations for the timings of the pulses have been defined). To perform Bloch oscillations, we load the atoms at time $t_{\mathrm{acc.}}$ in an optical lattice by adiabatically ramping up the laser intensity for $\tau_{\mathrm{adiab.}} = 500$ µs. Then, we implement N_{B} oscillations by accelerating the lattice during a time τ_B. The time τ_B is proportional to N_{B} and it corresponds in our experiment to $\tau_{\mathrm{osc}} = 12$ µs per oscillation unless otherwise specified. Finally, the lattice is adiabatically ramped down for an other 500 µs.

The detection scheme (**Extended Data Figure 1b**) is composed of three horizontal retro-reflected light-sheets that the atoms fall through successively. The first light-sheet is resonant with atoms in $|F = 2\rangle$ that emit fluorescence photons collected on a large-area photo-diode. A cache placed at the bottom of the light-sheet blocks the retro-reflection which leads to pushing the detected atoms away from the detection system. The remaining atoms in $|F = 1\rangle$ pass through a light-sheet that repumps them in $|F = 2\rangle$ and they are subsequently detected in a third light-sheet similar to the first one. The relative population of atoms in each state is then obtained from the collected fluorescence signals.

Theoretical phase shit at the output of the interferometer To maintain the resonance condition of the Raman transitions, the frequency difference ω_{R} between the lasers that drive them is carefully adjusted. In addition to the frequency difference shift $\delta\omega_R$ between the first and third $\pi/2$ pulses, we apply during the Ramsey sequences a ramp at rate β to compensate for gravity. Thus, the effective wave vector of Raman transitions varies during the interferometer which can induce a bias[35].

Treating this effect as a perturbation in the Lagrangian formalism[36] we obtain a modified version of equation (2):

$$\begin{aligned}\Phi = T_{\mathrm{R}}\Bigg[\epsilon_{\mathrm{R}} 2k_{\mathrm{R}}\left(\epsilon_{\mathrm{B}}\frac{2N_{\mathrm{B}}\hbar k_{\mathrm{B}}}{m} - gT\right) - \delta\omega_{\mathrm{R}}\Bigg] + \phi_{\mathrm{LS}} \\ + \frac{T_{\mathrm{R}}}{c}\Bigg[\beta\left(gT\left(\frac{T}{2}+T_{\mathrm{R}}\right) - v_0 T + \epsilon_{\mathrm{B}}\frac{2N_{\mathrm{B}}\hbar k_{\mathrm{B}}}{m}\left(t_{\mathrm{acc.}} + \tau_{\mathrm{adiab.}} + \frac{\tau_{\mathrm{B}}}{2} - T_{\mathrm{R}} - T\right)\right) \\ + 2k_{\mathrm{R}}\left(\frac{2N_{\mathrm{B}}\hbar k_{\mathrm{B}}}{m} - gT\right)\left(2v_0 - \frac{T_{\mathrm{R}} g}{2} + \epsilon_{\mathrm{B}}\frac{2N_{\mathrm{B}}\hbar k_{\mathrm{B}}}{m} - gT\right)\Bigg],\end{aligned} \tag{4}$$

where k_{R} is defined as the effective wave vector when the lasers frequency difference is set to address atoms at zero-velocity. This formula should be used in order to compute h/m from the central frequency determinations of the four spectra. However, because the additional term (second and third

lines) is independent of the direction of Raman beams, the determination of h/m from equation (3) remains valid provided that the value of Raman wave vector corresponds to the one resulting from addressing atoms at zero-velocity. Since we use this value, there is no correction associated to this effect.

Evaluation of uncertainty budgets Thanks to the high sensitivity of our atom interferometer, a wide range of systematic effects has been investigated and evaluated experimentally. Furthermore, we perform the measurements of h/m with various experimental parameters ($N_{\mathrm{B}}, T_{\mathrm{R}}, \tau_{\mathrm{B}}$, Raman lasers intensity). Parameters are listed on **Extended Data Table 1**.

As many systematic effects depend on the position or velocity of atoms, we implemented a Monte Carlo simulation of the experiment, in order to calculate those effects precisely. Notice that trajectories of the atoms during the measurement sequence are precisely controlled by mean of the atomic elevator. The Monte Carlo simulation is based on the calculation of atomic trajectories using the real-time sequence of the experiment. Quantities depending on the trajectory of the atoms (such as contrast of Rabi oscillation or efficiency of Bloch oscillations) were calculated and compared with experimental results to confirm the validity of the model.

Calculation of the final uncertainty The final value of h/m is obtain from hundreds of individual measurement of h/m. For each measurement, an uncertainty was calculated. This uncertainty has several origins that may be unique to this measurement (for example the uncertainty of the fit or the laser frequency measurement) or depend on the parameters of the measurement (for example light shift, gravity gradient) or common to all measurement (for example beam parameters). The `uncertainty` package of Python[37] is used to compute the weighted average value of h/m. The final uncertainty is a weighted quadratic sum of all the elementary source of uncertainties. The error budget is obtain by gathering those contributions depending on their origin.

Monte Carlo simulation In this simulation, each atom is described by an atomic wave packet with a mean momentum $\vec{p}(t)$, a phase $\phi(t)$ at its mean position $\vec{r}(t)$ and a real amplitude $a(t)$. The momentum $\vec{p}(t)$ and the position of the wave packet $\vec{r}(t)$ evolve using classical forces acting on the atom and the phase is calculated along this path. The sequence is split in different stages where the accumulated phase, the evolution of the trajectory and the amplitude are computed. Three kind of stages are considered: free fall in the gravity field, Raman transitions and Bloch oscillations.

During free fall, the amplitude remains constants, the trajectory is given by classical physics and the phase is computed using the action along the classical trajectory.

For Raman transitions, evolution is calculated in an accelerated frame where the Raman frequency is constant. Analytical solutions for a finite pulse duration in the momentum representation are used[38]. This allows to compute the amplitude and the phase. The displacement is calculated from the derivative of the phase with respect to the momentum.

For Bloch oscillations, the evolution is calculated in the frame of the lattice. In this frame the evolution is periodic and no displacement of the wave packet occurs. The phase evolution depends on three terms: i/ the phase due to the absorption and stimulated emission of N_B photons: $\phi_{\mathrm{ph}} = N_B(\phi_{\mathrm{up}}(x,t) - \phi_{\mathrm{down}}(x,t))$, where ϕ_{up} and ϕ_{down} are the phase of the two lasers of the lattice; ii/ the phase due to acceleration: $\phi_{\mathrm{acc}} = m(g-a)\tau_B/\hbar$, where a is the acceleration of the lattice and τ_B the total duration of the acceleration; and iii/ the phase due to the lattice ϕ_{latt}, which is calculated from the average energy of the atom in the first band in the tight binding limit:

$$\phi_{\mathrm{latt}} = \left(2\sqrt[4]{E_r^2 V_{\mathrm{up}} V_{\mathrm{down}}} + \left(\sqrt{V_{\mathrm{up}}} - \sqrt{V_{\mathrm{down}}}\right)^2\right)\frac{\tau_B}{\hbar} \tag{5}$$

where E_r is the recoil energy and $V_{\mathrm{up/down}}$ is the potential (light shift) of each individual laser of the lattice. From this energy, a classical force that acts on the atom is also calculated. The amplitude is calculated independently: the efficiency of Bloch oscillation, which depends on both the depth of the lattice and the magnitude of the acceleration, was taken from tables computed using an independent numerical simulation[39,40].

The analytical formula for Raman and Bloch evolution are obtained assuming that the laser beam used are plane waves. Generalisation to other beam was obtained by using formula with a plane wave that locally fits the phase of the laser (amplitude, phase and phase gradient). Those local parameters are obtained analytically when the simulation was performed with Gaussian beams. In the case of an arbitrary beam, numerical values were obtained using plane wave decomposition of the solution of the Helmholtz equation. Basically, we compute the Fourier transform $\tilde{A}(k_x, k_y, z_0)$ of the wavefront at position z_0. At any position, the complex amplitude is calculated using:

$$A(x,y,z) = \int e^{i(k_x x + k_y y + \sqrt{k^2 - k_x^2 - k_y^2}\, z)} \tilde{A}(k_x, k_y, z_0) dk_x, dk_y \tag{6}$$

and the recoil using

$$k_z(x,y,z) = \int \sqrt{k^2 - k_x^2 - k_y^2}\, e^{i(k_x x + k_y y + \sqrt{k^2 - k_x^2 - k_y^2}\, z)} \tilde{A}(k_x, k_y, z_0) dk_x, dk_y \tag{7}$$

The Monte Carlo simulation occurs as follows: an initial set of N wave packets (index i) is randomly calculated with a Gaussian distribution for both the position and velocity. For each wave packet, and for the two paths (labelled A and B) of the interferometer, the final amplitude $a_i^{A/B}$, position $\vec{r}_i^{A/B}$, momentum $\vec{p}_i^{A/B}$ and phase $\phi_i^{A/B}$ are calculated. The phase of the interferometer is then obtained from:

$$\Phi = \frac{1}{N}\sum_{i=1}^{N} a_i^A a_i^B \left(\phi_i^A - \phi_i^B + \frac{(\vec{p}_i^B + \vec{p}_i^A)\cdot(\vec{r}_i^B - \vec{r}_i^A)}{2\hbar}\right) \tag{8}$$

The simulation is run for each of the four spectra. The value of h/m is deduced using equation (3)

Frequency measurement The Bloch laser and of one of the Raman lasers are locked to a Fabry-Perot cavity. The cavity is itself locked to the $5S_1/2(F=3)-5D_5/2(F=5)$ two-photon transition in ^{85}Rb[41]. The frequencies of those two lasers are measured using a commercial frequency comb made by MenloSystems, which is referenced by a 100 MHz signal, referenced to the French National References of Time delivered by the LNE-SYRTE via a 3 km-long optical fiber link.

The **Extended Data Figure 2e** represents the Allan deviation of the measurement. In the short term, we observe variations in frequency up to 4 kHz related to temperature fluctuations caused by air conditioning (timescale of about 200 seconds). The record of the interferometer fringes for a single h/m determination lasts approximately 300 seconds. For the h/m computation, we take the average of the measurements and assign to each value an uncertainty of ± 4 kHz. Note that the contribution of this uncertainty on the error budget is negligible as the laser frequencies determination for two consecutive h/m determination are independent variables, the systematic error of the frequency comb being insignificant.

The measurement is continuously performed as long as the frequency comb laser remains locked. When the measurement of the frequency was not performed, but h/m measurements were taken, we estimated the frequency of the lasers using a linear interpolation and increase the uncertainty of the determination to ± 8 kHz. This uncertainty is common to a period over which the laser frequencies were not measured, *i.e* they do not average out. Because most of the time the frequency measurement was performed, these uncertainties contribute to a negligible amount to the error budget. The weighted mean uncertainty of the lasers frequencies during this period is about 1.2 kHz per laser, leading to a contribution to the error budget of $(0 \pm 6.0) \cdot 10^{-12}$.

Gravity gradient The phase shift induced by a linear gravity gradient γ writes:

$$\Phi_{\text{grav. grad}} = 2\epsilon_{\mathrm{R}} k_R T_{\mathrm{R}} T \gamma z_m, \tag{9}$$

where z_m is:

$$\begin{aligned} z_m = z_0 + \frac{v_0}{2}\left(T + T_{\mathrm{R}}\right) - \frac{T\epsilon_R \hbar k_{\mathrm{R}}}{m} - g\left(\frac{T^2}{6} + \frac{T T_{\mathrm{R}}}{4} + \frac{T_{\mathrm{R}}^2}{6}\right) \\ + \frac{N_{\mathrm{B}}\hbar k_{\mathrm{B}}}{Tm}\left(\frac{T_{\mathrm{R}}^2}{12} + \frac{\tau_{\mathrm{B}}^2}{12} + \left(T + \frac{T_{\mathrm{R}}}{2} - t_{\text{acc.}} - \tau_{\text{adiab.}} - \frac{\tau_{\mathrm{B}}}{2}\right)^2\right) \end{aligned} \tag{10}$$

We use the atomic elevator to position the atoms in the interferometer zone. The nice feature of this method is that we can choose v_0 and z_0 so that the average position for the four spectra (ϵ_{R}, ϵ_{B}) is the same, thus mitigating the effect of the gravity gradient. We estimate that we can achieve a precision below 100 μm, leading to uncertainty on h/m below 10^{-12}. We discovered after the measurement campaign that a mistake was present on the calculation of the trajectories for the spectra with 500 BOs, leading to a distance of 2.31 mm between the upwards and downwards acceleration trajectories. Using a standard gravimeter configuration of our experiment, we have measured a gravity gradient of $(2.25 \pm 0.3) \times 10^{-6}$ s^{-2}. This leads to an overall correction on h/m of $-1.27 \pm 0.17 \times 10^{-11}$.

Earth rotation Coriolis acceleration, resulting from Earth rotation, induces a phase shift which depends on the individual velocity $\vec{v}$ of the atoms. It is given by:

$$\Phi_{\text{Coriolis}} = 2T_{\mathrm{R}} T \vec{k}_R \cdot \left(\vec{\Omega}_E \times \vec{v}\right), \tag{11}$$

where $\vec{\Omega}_E$ is the vector describing the Earth rotation. Its effect is expected to cancel because of the symmetry of the atomic velocity distribution. However, a residual phase shift can occur because of imperfection of the detection system[42]. Thus, we compensate for effect of Earth rotation by using piezo-electric transducers on the retro-reflection mirror[21,43]. We perform the calibration of the Coriolis compensation parameters by maximizing the contrast of a 700 ms long interferometer (see **Extended Data Figure2b**).

We have measured h/m with compensation of the Earth rotation and without. The result of this survey is displayed on **Extended Data Figure2c**, and shows that the Earth rotation induces a $(2.6 \pm 2.1) \times 10^{-10}$ shift of h/m. We estimate the accuracy on the rate of the compensation ramps to $\pm 7\%$, which yields an uncertainty on h/m of $0 \pm 2.3 \cdot 10^{-11}$ (uncertainty obtained from the standard deviation calculated to the second order). This experimental value sets a limit on all effect related to Earth rotation (Coriolis force and Sagnac effect).

Beams alignment The beams are aligned by an automatic procedure every 10 records of the four spectra (about 45 minutes). The alignment of the Bloch beams is done by maximizing the coupling of the beam down into the lower fiber. The Raman beams alignment is done by optimizing the retro-reflection in the upper fiber. Assuming that alignments are independent and that drifts are negligible during the 45 minutes between two alignments, one can calculate the standard angular deviation from the shot to shot alignment. We found between the two Raman beams $\sqrt{\langle \theta_{\mathrm{R}}^2 \rangle} \simeq 3.7\,\mu\text{rad}$ and between the two Bloch beams $\sqrt{\langle \theta_{\mathrm{B}}^2 \rangle} \simeq 2.6\,\mu\text{rad}$. The correction on h/m given by $(\theta_B^2 + \theta_R^2)/2$ is equal to 1.0×10^{-11}. We took a conservative uncertainty of 1.0×10^{-11}.

Wave front corrections Using the paraxial approximation, for any scalar field $\mathcal{E}(x, y, z_0) = A(x, y, z_0) e^{i\phi(x,y,z_0)}$ at the position z_0, one can calculate the local wave vector:

$$k_z = k\left(1 - \frac{1}{2}\left|\left|\frac{\vec{\nabla}_\perp \phi}{k}\right|\right|^2 + \frac{1}{2k^2}\frac{\Delta_\perp A}{A}\right) \tag{12}$$

where the gradient and Laplacian are taken along the x et y directions. This formula is a generalisation of analytical formula obtained for Gaussian beams.

Using a shearing interferometer, we have measured the wave curvature of the beam and estimate it to $(0.9 \pm 0.3) \times 10^{-3}$ m^{-1} for both beams. The term in Laplacian (associated with the Gouy phase) has been calculated from pictures taken with a CCD.

Equation (12) is used in the Monte Carlo simulation in order to compute the local wave vector at the position of atoms. The correction depends on the size of the cloud and therefore on the parameters used. We obtain an average value for the curvature leading to an additional correction of $(1.3 \pm 0.6) \times 10^{-11}$.

In order to compute precisely the Gouy phase correction, we took several pictures of each beam at different distance from the collimator corresponding to the position of the clouds in the interferometer. In the experiment, the precision on the overlap of the laser beams is less than 10% of the waist. This is not as precise as the beam alignment (less than 10^{-5}). We have not implemented an automatic procedure for this less sensitive alignment.

The adjustments of the overlap between the upward and downward beams and the overlap between the atomic cloud and the laser beams were carefully made at the beginning of the measurement and re-checked if we observe a drop in the contrast of atomic fringes or in the number of atoms. Our method for controlling beam overlap consists in using, during the alignment procedure described above, a razor blade mounted on a micrometric translation. This technique usually used to estimate the waist of laser beam allows us to superpose the centers of laser beams at better than 10%, so we took an uncertainty of $\pm 500\ \mu$m for this overlap.

To align the laser beam overlap with the atomic cloud, we use Rabi oscillations with the two co-propagating Raman beams (downward Raman beams). The procedure consists in minimizing the pulse duration that satisfies the π condition by laterally displacing the laser beams (the fiber is placed on a micro-metric translation). Of course, at each lateral position, the injection of the beams into the fibers is re-optimized.

Independently, simulations were performed with different sets of parameters of the overlap of the beams between themselves and with the atomic cloud. We took the standard deviation of those simulations to estimate the uncertainty of the generalized Gouy correction. We obtained an uncertainty of 2.9×10^{-11}.

In the experiment, the survival probability $P(I)$ of an atom in the Bloch acceleration process depends on the local intensity I of the laser. The effective wave vector is equal to:

$$k_z^{\text{eff}} = \frac{\langle P(I(x,y,z_0))k_z(x,y,z_0)\rangle}{\langle P(I(x,y,z_0))\rangle}, \tag{13}$$

where the average is taken over the spread of the cloud. Correlation between the atomic distribution and laser intensity lead to a systematic effect identified in [23]. In order to precisely characterize this effect, we ran the experiment using a reduced value of I so that there is a stronger correlation between survival probability and intensity. The **Extended Data Figure 4b** displays the result of this experiment and the curve obtained with the Monte Carlo simulation. The parameter of the simulation were adjusted so that both the variation of the number of atoms and the variation of relative recoil match the experimental data. Furthermore, we had to add a small noise (2% at a scale of $50\mu m$ to the pictures recorded with a CCD camera). We observed that for a reduction of 50% of the intensity of the laser, there is a reduction of 40% of the number of atoms and a systematic effect of about 1 ppb. Under the standard condition (90% of the intensity of the maximum intensity), the calculated correction is $(7.8 \pm 3.8) \times 10^{-11}$.

Quadratic Zeeman effect We have measured the magnetic field $B(z)$ along the vertical axis in the interferometry area using the $|F = 1,\ m_F = 1\rangle \rightarrow |F = 2,\ m_F = -1\rangle$ transition and observe peak-to-peak variation smaller than 50 nT. This measurement is displayed on **Extended Data Figure 2d**.

The phase shift ϕ_B induced by the magnetic field can be calculated by integrating along the trajectory the variation of the Lagrangian due to the presence of the magnetic field,

$$\frac{\phi_B}{2\pi} = \frac{K}{2}\int_{t_{\text{interf.}}}^{\text{interf.}+T+T_{\text{R}}} s(t)B(z(t))^2 dt, \tag{14}$$

where $K = 575.15$ Hz G^{-2} and $s(t) = 1$ if the atom is in $|F = 1, m_F = 0\rangle$ or $s(t) = -1$ if it is in $|F = 2, m_F = 0\rangle$. Using the precise computation of the atomic trajectories for each interferometer and the measured magnetic field along the interferometer area, we obtain relative corrections on h/m that are below 10^{-12}. Thus, we apply a conservative uncertainty of 10^{-12} and no correction.

One photon light-shift The one photon differential light shift is negative and proportional to the intensity I seen by atoms:

$$\delta_{\text{L.S}} = -\frac{I}{I_s}\frac{\Gamma^2 \nu_{\text{HFS}}}{8\Delta^2} \tag{15}$$

where Γ is the natural linewidth of the rubidium D2 line, I_s its saturation intensity and Δ the detuning of the Raman laser with respect to the D2 line.

During the interferometer, the intensity of each Raman pulse is increased linearly with respect to time in order to compensate for the expansion of the cloud and keep a constant average intensity. Typically, we increase by 10% the intensity between the first and last pulse. This number corresponds to the laser intensity ramp that reduces the velocity-dependent phase shift during Raman transitions, induced by the unbalance of the average internal intensity between Raman pulses [25]. Calibration of the slope of the intensity ramp was performed under the same experimental conditions as those of the measurement of the ratio h/m in order to ensure the same detection efficiency.

Effect of light shift are similar for each spectrum and therefore should cancel between both the inversion of the direction of the Raman beams and of the Bloch acceleration. This compensation is not perfect for two reasons: i/ the temporal sequence being different, the size of the cloud is slightly different when the Bloch acceleration is inverted and ii/ the retro reflected beam, which contributes twice, is different when the direction of the

Raman beams is inverted. The Monte Carlo simulation is used to compute precisely the effect of the light shift and results are shown on **Extended Data Figure 4c**. Those results are plotted as a function of the velocity of the cloud (detuning δ_D with respect to the resonance): indeed, there a velocity-dependent phase shift induced by the Raman transitions [38] which has a dispersive shape. This effect has been studied in [25]. It depends on the intensity and is part of the simulation.

Using the results of the Monte Carlo simulation at zero Doppler detuning, we compute the dependency of the systematic error with respect to the light shift imbalance ξ. The error then writes:

$$\frac{\Delta\left(h/m\right)}{h/m} \simeq \left(\kappa_1 + \kappa_2 \left\langle \delta_D \right\rangle\right) \xi, \tag{16}$$

where $\langle \delta_D \rangle$ is the average Doppler shift of the atomic distribution. The value of κ_1 and κ_2 are extracted from the Monte Carlo simulation for each of the eight configurations used (see Extended Data Table 1a). We estimate the light shift imbalance ξ to 0.1 ± 0.1. We estimate that we compensate the light shift at the velocity selection stage at $\pm 10\%$ of 2 kHz. As a consequence we set δ_D at 0 ± 200Hz. Value for each configuration is displayed on Extended Data Table**2**.

Two-photon light shift In our experiment, the two Raman lasers are transported to the vacuum cell using the same fiber (the counterpropagating configuration is then achieved by retro-reflecting one of the two lasers). Thus, co-propagating Raman transitions induce a two-photon light shift between the two hyperfine levels that writes:

$$\delta_{2\gamma} = -\frac{\Omega^2}{2\delta_{\mathrm{copro.}}}, \tag{17}$$

where Ω is the Rabi frequency of the Raman transitions, and $\delta_{\mathrm{copro.}}$ the detuning of the co-propagating transitions mainly due to Doppler effect. Because $\delta_{\mathrm{copro.}}$ changes sign with the direction of Raman beams, this effect does not cancel with this inversion. In our configuration this light shift evaluates at a maximum of 5 Hz. The precise estimation of this effect is performed using the Monte Carlo simulation. The uncertainty associated to this correction comes from the knowledge of the Rabi frequency of the pulses that we estimate to 10%. Corrections for each configuration are given in Extended Data Table**2**. The correction on h/m is $(-11.5 \pm 4.7) \times 10^{-11}$.

Phase shift in Raman Phase Lock Loop The setup used to control the frequency difference $\omega_{\mathrm{R}}(t) = \omega_{\mathrm{HFS}} + \delta\omega_{\mathrm{RF}}(t)$ between the two Raman lasers is presented on **Extended Data Figure 3a**. It is based on a phase-lock loop (PLL) that control precisely the phase of the beat note signal between the two lasers. The PLL is controlled with a radio-frequency generator at frequency $\omega_{\mathrm{C}} + \frac{\delta\omega_{\mathrm{RF}}(t)}{8}$. Before the PLL, the beat note signal is mixed with a microwave generator at the frequency $\omega_{\mathrm{HFS}} - 8\omega_{\mathrm{C}}$. There is a ratio 8:1 between the radio-frequency generator and the beat note.

To compensate for the Doppler shift induced by gravity, we implement a frequency ramp of rate $\beta \approx \pm 25$ MHz/s during the Ramsey sequences of the interferometer where the sign of the ramp is dictated by the direction of Raman beams ϵ_{R}. Any delay δt in the PLL system, induces a shift $\beta\delta t$ in the frequency seen by atoms. A constant delay cancels over the interferometer sequence — however because of the frequency shift between the two Ramsey sequences, this delay varies and a phase error appears.

To mitigate the bias induced by this effect, we have implemented a symmetric configuration (**Extended Data Figure 3b**) by changing the frequency offset ω_{C} with the direction of Raman beams. Precisely, we impose that $8\omega_{\mathrm{C}} + \frac{\delta\omega_{\mathrm{RF}}(t_{\mathrm{interf.}}) + \delta\omega_{\mathrm{RF}}(t_{\mathrm{interf.}}+T) + \epsilon_R \beta T_{\mathrm{R}}}{2}$ is the same when the direction of Raman is inverted, so that the optical phase lock loop works in similar conditions.

However an independent measurement of the phase of the beat note signal revealed an imperfect cancellation at the mrad level. We suspect that this residual phase comes from a non-linear response of the phase comparator of the PPL. We perform this measurement by demodulating the beat note signal and recording it on a 100 MHz bandwidth oscilloscope (Tektronix DPO 3014). The beat note signal is lowered in frequency by mixing it with the signal of an additional microwave generator. The pulsation of this generator is set at the average $\langle \omega_{\mathrm{R}} \rangle$ of the interferometry sequence so that the signal on the oscilloscope is symmetric. The time base of the oscilloscope is calibrated by analysing the signal of a 10 MHz reference.

The beat note signal is demodulated for each pulse by computing its two quadrature with a numerically computed signal. We obtain for a single interferometric sequence the contribution of the phase of the Raman lasers using the usual formula $\phi_4 - \phi_3 - \phi_2 + \phi_1$ where the subscripts refer to the pulse order. An alternative analysis based on curve fitting of the beat note signals yields identical results.

For a single determination of h/m (see Fig. 3a), we obtain for each spectrum a collection of phase shift estimation. We compute the applied phase correction by taking the average of this collection and an uncertainty deduced from its standard deviation. The correction is accounted for in the interferometric phase (equation 2) and propagated to the value of h/m.

We have checked that the oscilloscope does not induce a bias by reducing its bandwidth to 20 MHz and did not detect shifts at the level of 0.01 ppb on h/m. Moreover, we have studied the relationship between the phase of the beat note and the interferometric measurement in the following way: using 600 determinations of h/m performed continuously over $\approx$ 60 hours, we divided the set into six quantiles sorted by the beat note phase. For each quantile, we averaged this phase and the interferometric phase. **Extended Data Figure 3c** displays the relationship between these two quantities and shows that their fluctuations are identical (slope of 1).

Experimentally, we have also checked that this method can compensate the phase shift observed when filters with different cutoff frequencies are inserted in the PLL.

We evaluated the related correction to h/m, which depends on the interferometer parameters N_{B} and T_{R}. Note that the effect of a phase shift $\delta\Phi$ scales as $\delta\Phi/T_{\mathrm{R}}$ on h/m. For $N_{\mathrm{B}} = 500$, we find a correction on h/m of $\approx -9 \cdot 10^{-10}$ for $T_{\mathrm{R}} = 10$ ms or 20 ms which shows that the phase shift induced by frequency ramps depends on their duration. Moreover, we find a reduced effect for $N_{\mathrm{B}} = 250$ at $\approx -6 \cdot 10^{-10}$ which is expected

because the frequency difference between the first and third pulse is ~ 7.5 MHz compared to 15 MHz for $N_{\mathrm{B}} = 500$. We then find a correction to h/m of $(-82.1 \pm 1.2) \cdot 10^{-11}$. The uncertainty includes a conservative uncertainty of 0.01 ppb on the phase measurement with the oscilloscope.

Methods references

34. Andia, M., Wodey, É., Biraben, F., Cladé, P. & Guellati-Khélifa, S. Bloch oscillations in an optical lattice generated by a laser source based on a fiber amplifier: Decoherence effects due to amplified spontaneous emission. *J. Opt. Soc. Am. B* **32**, 1038–1042 (2015).

35. Wolf, P. & Tourrenc, P. Gravimetry using atom interferometers: Some systematic effects. *Physics Letters A* **251**, 241–246 (1999).

36. Pippa Storey & Claude Cohen-Tannoudji. The Feynman path integral approach to atomic interferometry. A tutorial. *J. Phys. II France* **4**, 1999–2027 (1994).

37. Lebigot, E. O. Uncertainties: A Python package for calculations with uncertainties.

38. Weiss, D. S., Young, B. C. & Chu, S. Precision measurement of h/m Cs based on photon recoil using laser-cooled atoms and atomic interferometry. *Appl. Phys. B* **59**, 217–256 (1994).

39. Glück, M., Kolovsky, A. R. & Korsch, H. J. Wannier–Stark resonances in optical and semiconductor superlattices. *Physics Reports* **366**, 103–182 (2002).

40. Cladé, P., Andia, M. & Guellati-Khélifa, S. Improving efficiency of Bloch oscillations in the tight-binding limit. *Phys. Rev. A* **95**, 063604 (2017).

41. Touahri, D. *et al.* Frequency measurement of the two-photon transition in rubidium. *Optics Communications* **133**, 471–478 (1997).

42. Louchet-Chauvet, A. *et al.* The influence of transverse motion within an atomic gravimeter. *New Journal of Physics* **13**, 065025 (2011).

43. Hogan, J. M., Johnson, D. M. S. & Kasevich, M. A. Light-pulse atom interferometry. In Arimondo, E., Ertmer, W., Schleich, W. & Rasel, E. (eds.) *Procedding of the International School of Physics Enrico Fermi Course CLXVIII on Atom Optics and Space Physics*, 411 (IOS Press Oxford, 2008).

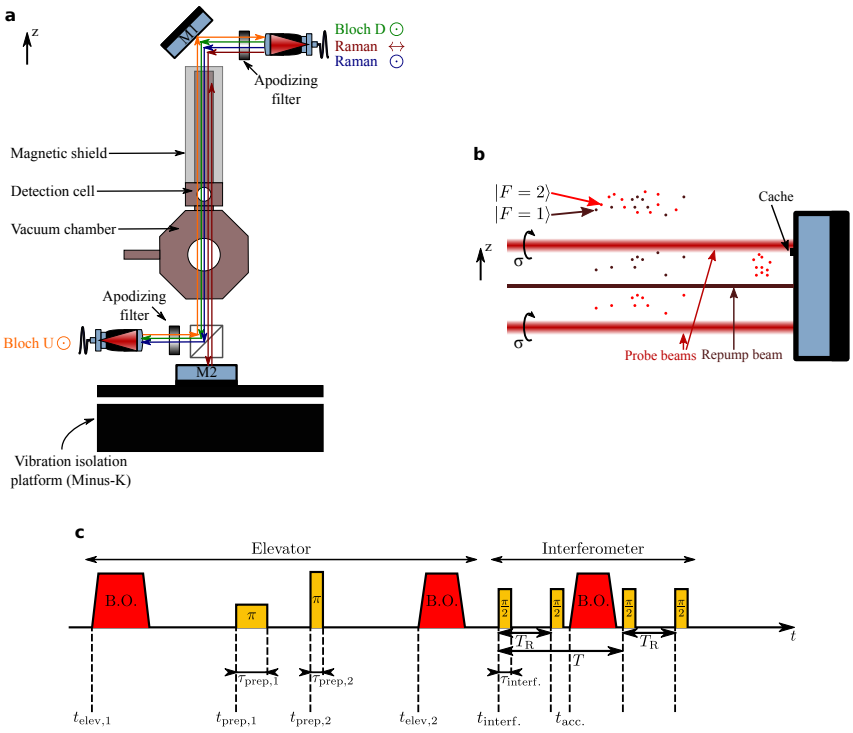

Extended Data Figure 1: **Laser beam setup and detection. a** Schematics of the vacuum cell and of the laser beams used for Raman transition and Bloch oscillation. **b** Schematics of the detection setup. **c** Light-pulse sequence implemented for the measurement protocol.

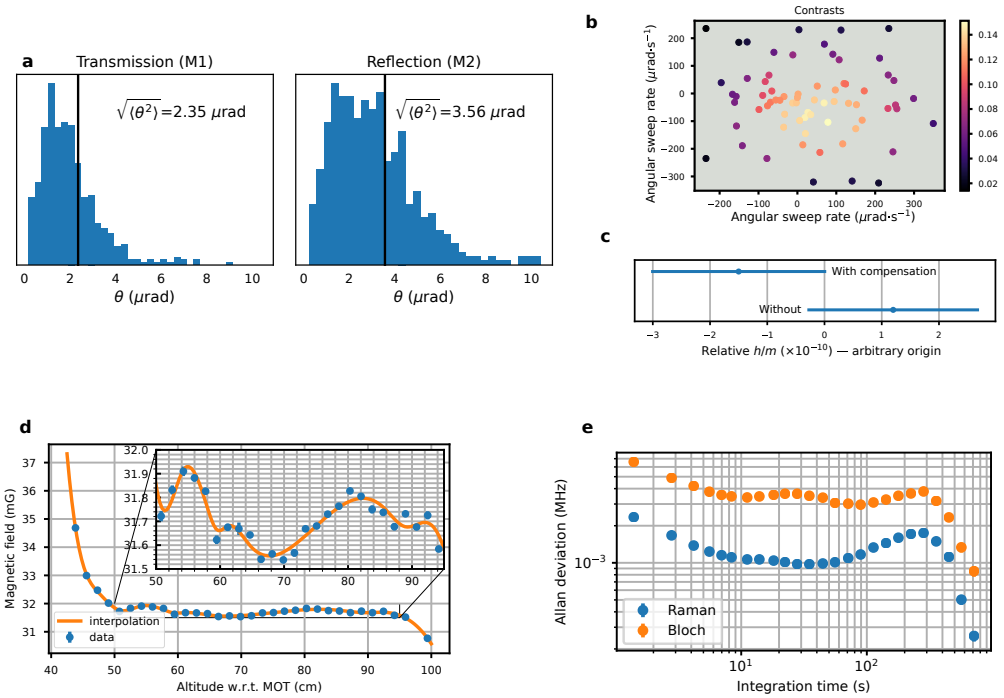

Extended Data Figure 2: **Data on the control of the laser beams alignment and the magnetic field. a** Distributions of the shot to shot variations of the auto-alignment procedures for mirrors M1 and M2 (see extended data figure 1a).**b** Scatter of the the contrast with respect to the sweep rates of the piezoelectric transducer of the mirror mounts (M2) for a 700 ms-long interferometer. **c** Integrated h/m raw determinations with and without Earth rotation compensation. Each point correspond to 400 sets of 4 spectra. The total interrogation duration is 60 hours. **d** Blue: measurement of the magnetic field obtained by measuring the resonance of the magnetically sensitive $|F = 1, m_F = 1\rangle \rightarrow |F = 2, m_F = -1\rangle$ transition. Orange: interpolation used for the modelling of the systematic effect. **e** Allan deviation of the frequency measurement.

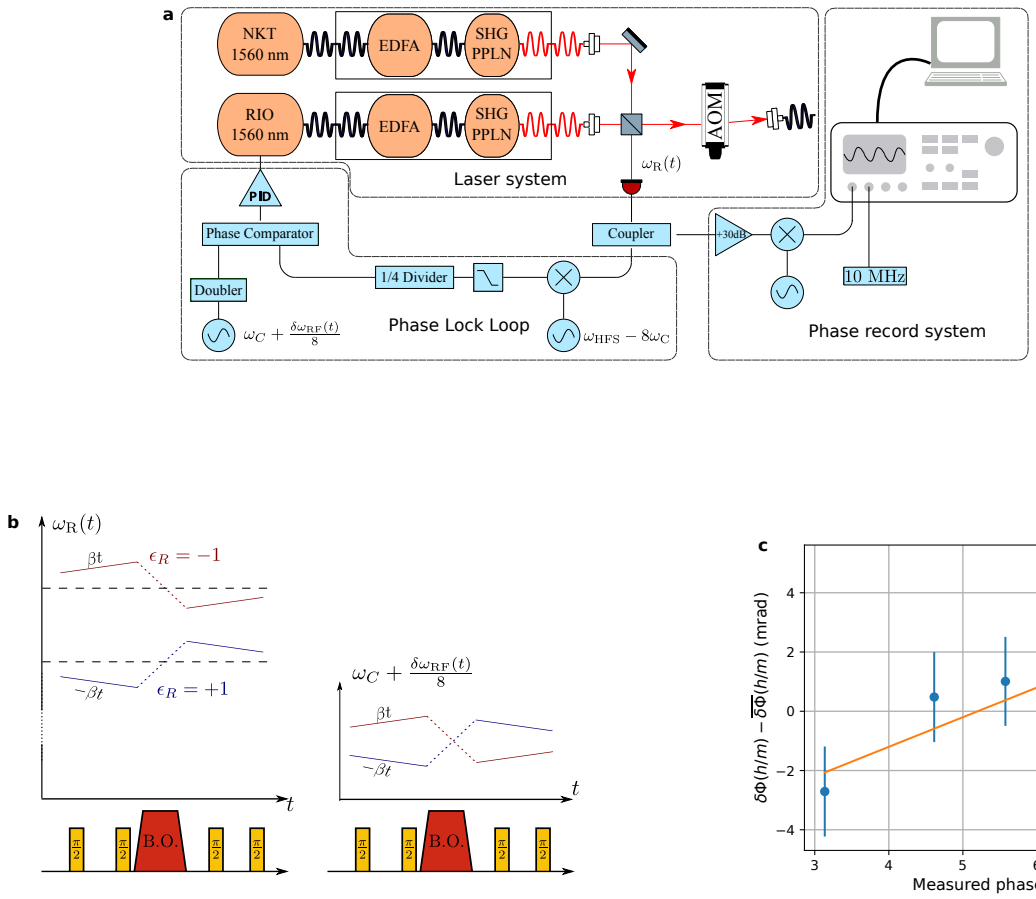

Extended Data Figure 3: **Frequency control of Raman lasers. a** Scheme of the Raman phase lock system. Top left: laser arrangement to extract a beat note between the two lasers. Bottom left: RF chain for the phase lock. Right: Setup for the measurement of the phase between the two lasers. **b** Frequency of the RF generator of the PLL for each Raman direction (red and blue lines) ω_C is changed with the Raman direction (right) in order to obtain symmetrized ramps. **c** Averaged interferometric phase with respect to the averaged correction deduced from the phase of the beat note.

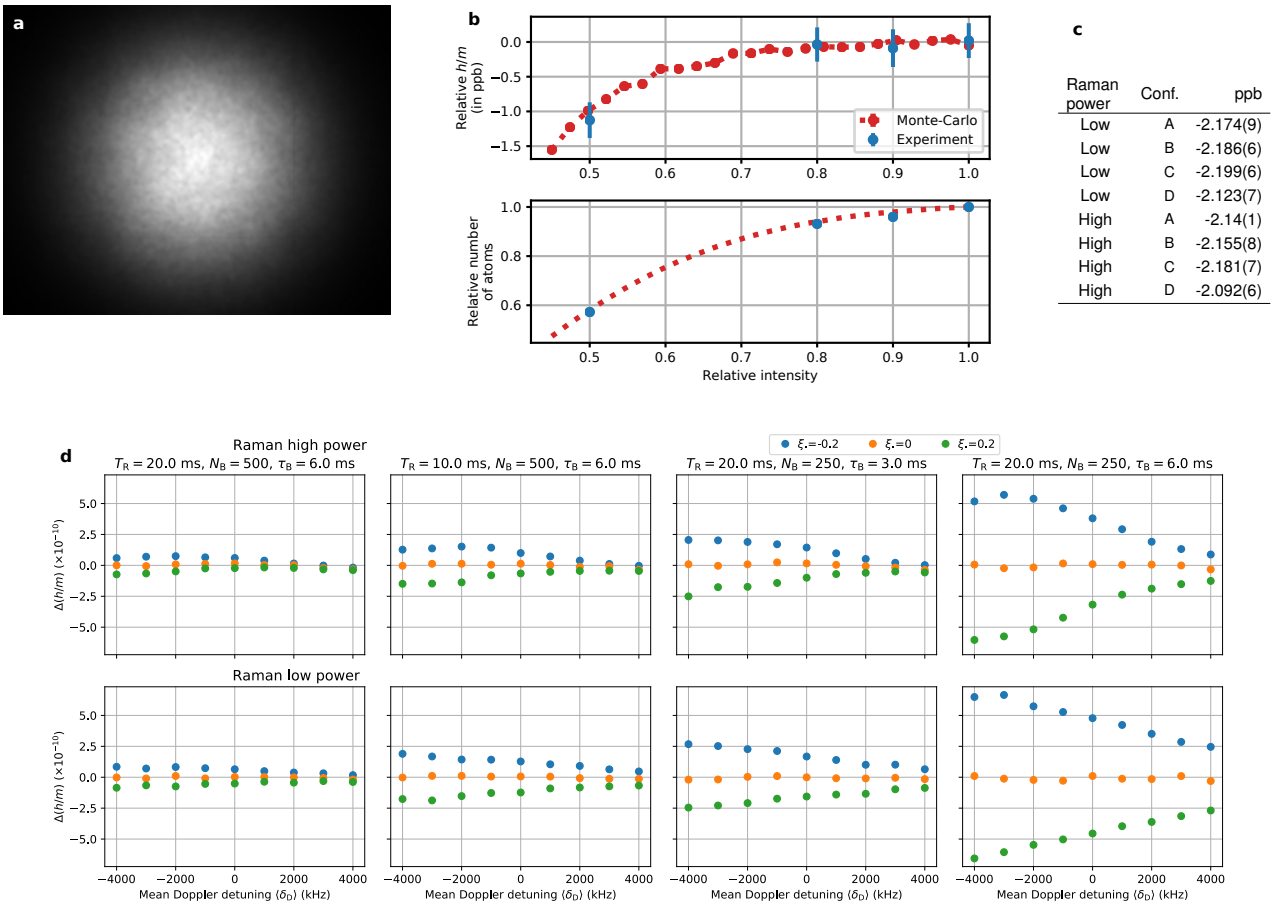

Raman power	Conf.	ppb
Low	A	-2.174(9)
Low	B	-2.186(6)
Low	C	-2.199(6)
Low	D	-2.123(7)
High	A	-2.14(1)
High	B	-2.155(8)
High	C	-2.181(7)
High	D	-2.092(6)

Extended Data Figure 4: **Analysis of the effect of local fluctuations in laser intensity.** **a** Typical intensity profile of the laser beam. **b** Characterisation of the short scale noise on the beam intensity. The intensity of the laser used for Bloch oscillation is reduced, leading to losses of atoms in the experiment (bottom graph). This induces a systematic effects on the recoil measurement (upper graph). In order to match the experimental data with the Monte Carlo simulation, we had to add a small noise (2% at a scale of $50\mu m$ to the pictures recorded with a CCD camera). **c** Correction from the intensity profile calculated for each configuration. Uncertainty displayed are only the independent ones obtained from the Monte Carlo simulation. **d** Results of the Monte Carlo simulation for the estimation of the effect of the one photon light shift, for different initial velocity and Raman inversion compensation (orange points: perfect compensation, blue and green points: one photon light shift are greater by 20% for one or the other Raman direction). The simulation was performed for all interferometer configuration (top: Raman high power, bottom: Raman low power) and different (T_{R}, N_{B}, τ_B) from left to right.

Extended Data Table 1: **Time sequence data.** Parameters used for the data collection for the different configuration and spectra. The times are indicated with respect to the release of the atomic cloud from the optical molasses. Legend of configurations : Ⓐ $T_{\mathrm{R}} = 20\mathrm{ms}$, $N_{\mathrm{B}} = 500$, $\tau_{\mathrm{B}} = 6\mathrm{ms}$; Ⓑ $T_{\mathrm{R}} = 10\mathrm{ms}$, $N_{\mathrm{B}} = 500$, $\tau_{\mathrm{B}} = 6\mathrm{ms}$; Ⓒ $T_{\mathrm{R}} = 20\mathrm{ms}$, $N_{\mathrm{B}} = 250$, $\tau_{\mathrm{B}} = 3\mathrm{ms}$; Ⓓ $T_{\mathrm{R}} = 20\mathrm{ms}$, $N_{\mathrm{B}} = 250$, $\tau_{\mathrm{B}} = 6\mathrm{ms}$. Legend of spectra : Spectrum 1: $\epsilon_R = +1$, $\epsilon_B = +1$; Spectrum 2: $\epsilon_R = -1$, $\epsilon_B = +1$; Spectrum 3: $\epsilon_R = +1$, $\epsilon_B = -1$; Spectrum 4: $\epsilon_R = -1$, $\epsilon_B = -1$

Configuration		Ⓐ	Ⓑ	Ⓒ	Ⓓ	
T_R		20	10	20	20	ms
N_B		500	500	250	250	BOs
τ_{osc}		12	12	12	24	µs
T				32.9		ms
$t_{\mathrm{elev,1}}$				9		ms
$N_{\mathrm{elev,1}}$				+650		BOs
$t_{\mathrm{prep,1}}$				110		ms
$\tau_{\mathrm{prep,1}}$				189		µs
$t_{\mathrm{prep,2}}$				120		ms
$\tau_{\mathrm{prep,2}}$				63		µs
$t_{\mathrm{elev,2}}$	Spectra 1, 2			154.910		ms
	Spectra 3, 4	131.528	131.946	137.492	136.984	
$N_{\mathrm{elev,2}}$	Spectra 1, 2	-1185	-1010	-1185	-1185	BOs
	Spectra 3, 4	-635	-515	-735	-735	
$t_{\mathrm{interf.}}$				175		ms
$\tau_{\mathrm{interf.}}$	Raman power: Low			80		µs
	Raman power: High			35		
$t_{\mathrm{acc.}}$				197.9		ms

Extended Data Table 2: **Light shifts -** Data computed with the Monte Carlo simulation for the different configurations: correction parameters of the light shift imbalance over the Raman direction (κ_1) and atomic mean velocity (κ_2); relative corrections to h/m due to the one photon light shift; correction on h/m induced by two-photon light shifts during Raman pulses. Configurations are described on extended data Table **1**

Power	Conf.	κ_1 ($\times 10^{-10}$)	κ_2 ($\times 10^{-13}$ Hz^{-1})	One-ph. corr. ($\times 10^{-11}$)	Two-ph. corr. ($\times 10^{-11}$)
Low	Ⓐ	-2.1	0.52	2.1 ± 2.1	-12.2 ± 3.7
Low	Ⓑ	-4.1	1.3	4.1 ± 4.1	-27.2 ± 5.9
Low	Ⓒ	-6.1	1.6	6.1 ± 6.1	-7.0 ± 3.0
Low	Ⓓ	-17	4.2	17 ± 17	-3.6 ± 2.7
High	Ⓐ	-2.9	0.48	2.9 ± 2.9	-39.3 ± 8.1
High	Ⓑ	-6.3	0.79	6.3 ± 6.3	-88.2 ± 17.8
High	Ⓒ	-8.1	1.3	8.1 ± 8.1	-27.4 ± 5.8
High	Ⓓ	-23	2.6	23 ± 23	-18.0 ± 4.3